Uncertainty Quantification of the FUN3D-Predicted NASA CRM Flutter Boundary

Bret K. Stanford* and Steven J. Massey†

NASA Langley Research Center, Hampton, VA, 23681

A nonintrusive point collocation method is used to propagate parametric uncertainties of the flexible Common Research Model, a generic transport configuration, through the unsteady aeroelastic CFD solver FUN3D. A range of random input variables are considered, including atmospheric flow variables, structural variables, and inertial (lumped mass) variables. UQ results are explored for a range of output metrics (with a focus on dynamic flutter stability), for both subsonic and transonic Mach numbers, for two different CFD mesh refinements. A particular focus is placed on computing failure probabilities: the probability that the wing will flutter within the flight envelope.

I. Introduction

Typical aircraft design procedures stipulate that, among many other design constraints, the aeroelastic flutter boundary of a vehicle be 15% beyond the flight envelope, as measured by equivalent air speed. Such a flutter margin is essentially empirical,[1] and may in some cases be too conservative, and in others not conservative enough. Neither outcome is desirable: the former due to weight and performance penalties of an over-designed structure, the latter due to the catastrophic nature of the flutter failure mechanism. A preferable, though challenging, alternative to the 15% flutter margin is to 1) identify the numerous uncertain parameters, and their probabalistic representations, that may affect the flutter response of an aeroelastic system, 2) propagate those uncertainties through the system, 3) compute the probability that the wing will flutter within its flight envelope, and 4) determine if this probability is less than some acceptable probability of failure.

For transonic configurations, such as a transport aircraft, flutter behavior is severely complicated by the regions of mixed flow (i.e., a shock) over the wing: results computed without transonic and viscous effects will likely be inaccurate.[2] Solvers rooted in unsteady RANS-based CFD are very expensive, however, even for deterministic computations. This cost will increase if uncertainty quantification (UQ) is of interest, particularly for problems with a large number of random variables and strong nonlinearities, both of which are typical of transonic flutter.

A recent review article by Beran et al.[3] has summarized the current state-of-the-art in the UQ of aeroelasticity problems. Several papers are identified in the literature that propagate parametric uncertainties through CFD-based aeroelastic solvers: see Allen and Maute,[4] Beran et al.,[5] Hosder et al.,[6] Witteveen and Bijl,[7] Danowsky et al.,[8] Marques et al.,[9] and Nikbay and Kuru.[10] Each of these papers utilizes inviscid Euler solvers, rather than Navier-Stokes solvers (though Ref. 8 does not explicitly clarify). The work of Hosder et al.[6] is, in particular, closely emulated here. That paper quantifies the uncertainty in the transient modal response of the AGARD 445.6 test case in response to uncertain Mach number and angle of attack, using a nonintrusive polynomial chaos expansion (NIPC, or PCE), also known as point collocation. NIPC is a very simple and popular method for quantifying uncertainties, though the method (like many UQ tools) scales poorly with large numbers of random parameters and strong nonlinearities.

The same NIPC method utilized by Hosder et al.[6] is used here as well, though the method will be demonstrated on a more realistic aeroelastic configuration (the Common Research Model), with a higher fidelity solver (the RANS solver FUN3D[11]), and a larger number of random variables, including uncertain

*Research Aerospace Engineer, Aeroelasticity Branch, bret.k.stanford@nasa.gov, AIAA Senior Member.
†Research Aerospace Engineer, Aeroelasticity Branch, s.j.massey@nasa.gov, AIAA Senior Member.

structural variables. The applicability of sparse PC expansions,[12] which can help alleviate the curse of dimensionality, is explored as well.

UQ results are presented in three sections. First, the uncertain dynamic aeroelastic response is computed due to atmospheric random variables (RVs), for a coarse CFD mesh. Next, CFD grid convergence is explored through the lens of UQ, by considering these same random variables on a finer CFD mesh. Finally, a larger set of random variables are included on the coarse mesh, including atmospheric, structural, and inertial parameters.

II. Aeroelastic UQ Formulation

A. Common Research Model

All of the work in this paper is conducted on the conceptual wing-body-tail Common Research Model (CRM). The wing model developed in Ref. 13 is a rigid $1g$ flying shape suitable for aerodynamic analysis. An undeflected jig shape version (uCRM) developed in Ref. 14 is suitable for aeroelastic analysis and is used here. This transonic transport configuration has a wing span of 58.7 m, a mean aerodynamic chord of 7.0 m, an aspect ratio of 9, a taper ratio of 0.275, a sweep angle of 35°, a cruise Mach number of 0.85, and a cruise Reynolds number of $43{\cdot}10^6$.

The topology of the wingbox developed in Ref. 14 is also used here, seen in Fig. 1. This structure consists of an upper skin, a lower skin, a leading edge spar (located at 10% chord at the root and 35% at the tip), a trailing edge spar (60% at both the root and the tip), and 43 ribs oriented perpendicular to the leading edge. A carry-through structure is assumed to lie within the fuselage. All shell members (ribs, spars, skins) are outfitted with T-shaped stiffeners, where the flange is bonded to the shell members. The stiffeners are not modeled explicitly, but instead smeared into the shell stiffness properties. The entire wing structure is constructed of aluminum.

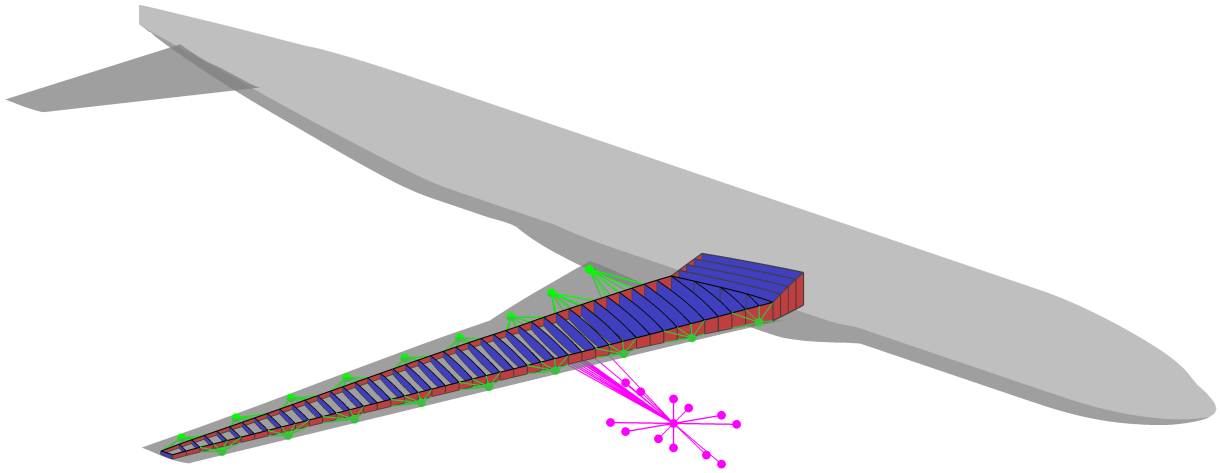

Figure 1. Wingbox, outer mold line, and lumped mass attachments of the uCRM.

The structure along the leading and trailing edges of the wing is not explicitly modeled, though an inertial effect is captured with a series of lumped masses attached to the wing box via interpolation elements. These masses, along with similar representations for the engine, are also shown in Fig. 1. The fuselage and tail of the CRM are modeled aerodynamically, but are assumed rigid. The engine is modeled inertially, but not aerodynamically.

B. Aeroelastic Analysis

The nominal stiffness properties of the uCRM wingbox, taken from Ref. 14, are shown in Fig. 2, in terms of the shell thickness, smeared stiffener thickness, and smeared stiffener height. A NASTRAN finite element model of the wingbox (composed of 10,500 quadrilateral shell elements) is used to compute the normal vibration modes (25 total) and the inertial force vector (self-weight) of the structure. Aeroelastic analysis is conducted via a modal structural solver internal to FUN3D, which is formulated in the same manner as

another aeroelastic CFD tool, CFL3D.[15] Structural inputs to FUN3D include the list of natural frequencies for each mode, prescribed modal damping, the inertial force vector written in modal coordinates, and mode shapes projected onto the CFD wing surface.[16]

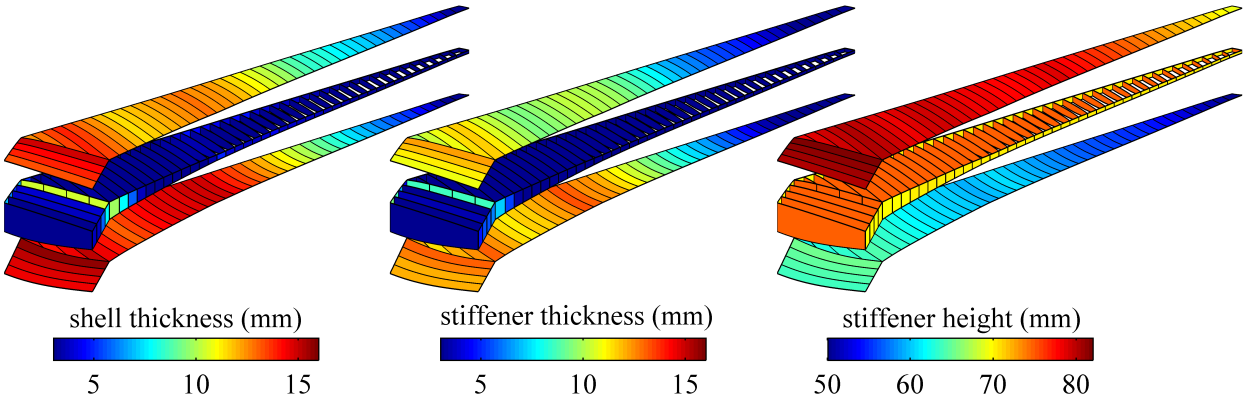

Figure 2. Thickness distribution throughout the wingbox.

Within FUN3D, the compressible Reynolds-averaged Navier-Stokes flow equations and the Spalart-Allmaras turbulence model are solved on semi-infinite tetrahedral volume grids with prismatic elements in the boundary layer. Two grids are considered here: a 3.1 million node mesh (coarse) and a 13.8 million node mesh (medium). For both grids, normal spacing of the first grid point off the vehicle is roughly $y^+ \approx 1$ throughout. The surface mesh of the coarse grid is shown in Fig. 3. Finer grids are not included here, due to the computational expense of the UQ analysis.

FUN3D computations are run in three stages. First, the flow is computed over a rigid wing. This rigid solution is then utilized as the initial condition for an unsteady flow analysis, with each modal damping ratio set to 0.99, to obtain a static aeroelastic solution. This converged solution is finally utilized as the initial condition for a second unsteady flow analysis, with modal damping ratios set to 0 (and some prescribed modal perturbation), to obtain a dynamic aeroelastic response history. CFD mesh deformation is obtained via a linear elasticity analogy.[17] For the dynamic aeroelastic results, the time step size is $3{\cdot}10^{-3}$ s (100 steps per 3 Hz cycle), with 30 subiterations per time step. For the computational resources allocated for this effort, roughly 15-20 aeroelastic cases (each comprising all three stages: rigid, steady, dynamic) could be completed within a week of wall time, for the coarse CFD mesh. For the medium mesh, only 5 cases could be completed within a week.

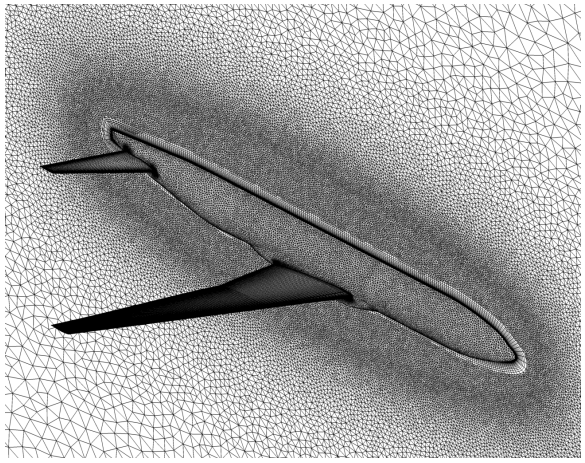

Figure 3. CFD surface mesh for the 3.1 million node grid.

C. Nonintrusive Polynomial Chaos

The method used in this work for uncertainty quantification is originally developed in Ref. 18 and will be briefly summarized here. Some aeroelastic output of interest, Y, is assumed to be represented by a weighted combination of basis functions written across the random variable space:

$$Y(\boldsymbol{\xi}) = \sum_{i=0}^{P} \alpha_i \cdot \Psi_i(\boldsymbol{\xi}) \tag{1}$$

where $\boldsymbol{\xi}$ is a vector of random variables written in standard normal space, Ψ_i is the i^{th} basis function, and α_i is the corresponding weight. For the normal random variables considered here, the basis functions are a total order expansion of Hermite polynomials, comprising $N_t = P + 1 = (n + s)!/n!/s!$ terms. n is the number of random variables in $\boldsymbol{\xi}$, and s is the desired order of the PCE. Further details regarding the mathematics of this assumed basis may be found in Refs. 18 and 19.

Y values are sampled at random locations (identified through Latin Hypercube sampling) throughout the random variable space, and then α_i terms are computed by solving a least squares problem. If the number of available samples is equal to or greater than N_t, Eq. 1 is an over-determined least squares problem. Ref. 18 recommends an oversampling ratio (ratio of the number of samples to N_t) of two. This sampling cost grows rapidly with increased n or s, however. An alternative method, used here, is to assume sparsity in the coefficient vector $\boldsymbol{\alpha}$, and solve Eq. 1 as a regularized (under-determined) least squares problem. The LASSO algorithm is used to solve this regularized problem,[20] potentially at an oversampling ratio much less than one. Tenfold cross validation is used to select the best solution of the LASSO-generated list of $\boldsymbol{\alpha}$ vectors.[21] Another potential method to reduce sampling cost is to enhance the point collocation process with gradients $dY/d\boldsymbol{\xi}$,[22] though analytical aeroelastic gradients (computed via the adjoint method) are not yet available in FUN3D.

Once the PCE expression of Eq. 1 is obtained, analytical expressions for the mean and standard deviation of Y are available,[19] as are Sobol indices (global nonlinear sensitivity parameters).[23] Alternatively, Monte Carlo sampling of the low-cost PCE may be conducted in order to obtain probability density functions (PDF), higher order moments, probabilities of failure, etc.

III. Deterministic Aeroelastic Response

First, the deterministic flutter boundaries of the uCRM, in terms of the matched-point dynamic pressure Q, are shown in Fig. 4 across a range of Mach numbers, for 0° and 2° angle of attack, for the coarse CFD grid. The 15% flutter margin (assumed dive speed of 185 m/s) is also shown. Up to a Mach number of 0.8, the flutter mechanism is driven by linear physics, with a weak dependence on angle of attack. Flutter does occur at a margin less than 15% at Mach 0.55, and then flutter Q gradually rises above the 15% margin with increased Mach number. Beyond Mach 0.8, mixed flow (shocks) begins to appear over the wing, causing stronger dependencies on angle of attack. At 0°, there is a pronounced flutter dip (minimum Q at Mach 0.9125), followed by a sharp rise in the flutter Q. At 2°, the flutter Q is more erratic, with less of a deviation from the linear extrapolation. It is finally noted that the medium CFD grid provides a good match to the coarse grid at the two selected cases in Fig. 4: 0° angle of attack, Mach 0.7 and 0.85.

Flutter boundaries in Fig. 4 are found by gradually increasing Q at a given Mach number and searching for instabilities in the oscillatory modal coordinate output. An example of this is shown in Fig. 5 at Mach 0.85 and 0° angle of attack, for four different dynamic pressures: both the static aeroelastic convergence ($t < 1$) and the subsequent dynamic results ($t > 1$) are shown. The mode 1 generalized coordinates (roughly corresponding to a first bending mode) are found to be representative of the wing aeroelastic behavior as a whole, and are used to assess stability. The lowest Q value in Fig. 5 is essentially a "wind-off" condition, and the mode vibrates at the first bending frequency (1.7 Hz), about a negative steady state deformation (due to the self-weight forces). Higher dynamic pressures allow the aerodynamic forces to overcome the self-weight loads, leading to positive steady state deflections, and an eventual loss of dynamic stability. Using a finer Q-step than shown in the figure, the flutter point is bracketed, and the linearly-interpolated cross-over point is plotted in Fig. 4.

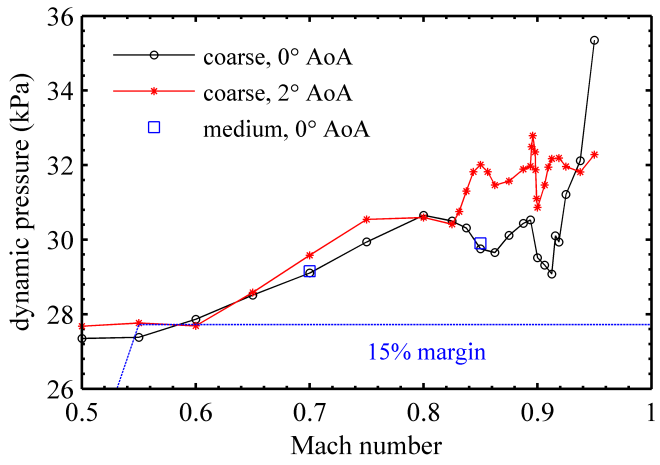

Figure 4. Deterministic flutter boundaries of the uCRM.

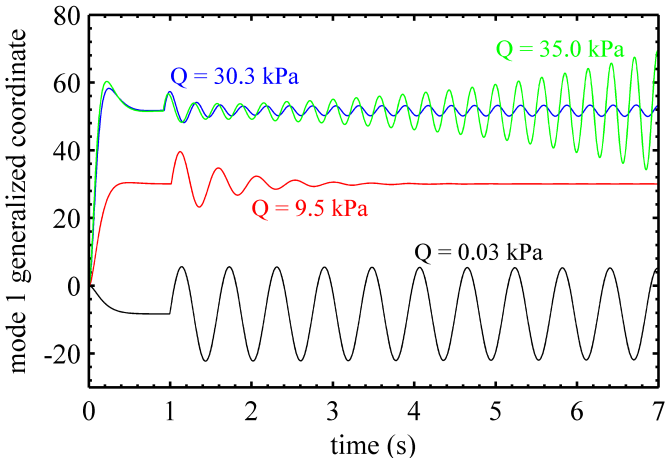

Figure 5. Aeroelastic time integration at Mach 0.85, 0° angle of attack.

IV. Atmospheric RVs, Coarse CFD Grid

Next, three uncorrelated normal random variables are utilized in $\boldsymbol{\xi}$: Mach number, dynamic pressure Q, and angle of attack. Mach number and Q are in reality dependent variables, but can be considered numerically uncorrelated by computing the flow density and speed to ensure a matched atmospheric point for a given Mach/Q combination. The only system output of interest (Y) in these results is the aeroelastic damping of the first generalized coordinate. Specifically, the last 8 peak-to-peak logarithmic decrements in the time history are averaged to form Y. For all cases explicitly examined, the decrements/increments are well-converged within these last 8 cycles.

Three PCEs are constructed, summarized in Table 1, expanded about the mean Mach numbers of 0.7, 0.825, and 0.875. The mean angle of attack is set to 0° (1° standard deviation), and the mean Q for each case corresponds to the associated deterministic flutter points in Fig. 4, with a 0.04 coefficient of variation (COV). Each RV is considered to be normally distributed. For the lower mean Mach number of 0.7, a low-order PCE is found to suffice, given the near-linear aeroelastic physics seen in Fig. 4. At Mach 0.875, the stronger aerodynamic nonlinearities in the flow require a higher-ordered PCE. The statistical output convergence at this transonic Mach number, as a function of polynomial order s, is shown in Table 2. Each PCE in this table is built with the same 168 samples, and the mean output μ_Y is nearly zero for all cases, as expected. For each value of s, the number of α_i terms in the total order expansion (N_t) is given, as well as the number of terms actually utilized by the sparse LASSO solver.

Probability density functions for the three PCEs in Table 1 are shown in Fig. 6, where an increase in

Table 1. Summary of PCEs constructed with atmospheric design variables.

order s	μ_{Mach}	σ_{Mach}	μ_Q	σ_Q	μ_{AoA}	σ_{AoA}
2	0.7	0.025	29.10 kPa	1.16 kPa	0.0°	1.0°
4	0.825	0.025	30.49 kPa	1.22 kPa	0.0°	1.0°
8	0.875	0.025	30.11 kPa	1.20 kPa	0.0°	1.0°

Table 2. Convergence of the mean μ and standard deviation σ of Y, at Mach 0.875.

order s	full N_t	sparse N_α	μ_Y	σ_Y
2	10	8	-0.002540074	0.032955274
3	20	17	-0.003158926	0.035441222
4	35	24	-0.003047019	0.035369842
5	56	33	-0.003346496	0.03727311
6	84	39	-0.002912447	0.037208744
7	120	41	-0.002937248	0.036669095
8	165	59	-0.003257288	0.037772292

Mach number increases the spread in the distribution (increases σ_Y), and the 0.875 Mach number case shows clear skewness from the transonic flow nonlinearities. Total sobol indices (global sensitivity parameters) are shown in Fig. 6 as well, for each atmospheric random variable. Overall, the dynamic stability is most strongly impacted by the dynamic pressure, but this impact wanes as Mach number is increased, and angle of attack becomes more predominant (Mach number also rises in importance, though to a much lesser degree). These results echo the results of Fig. 4, where subsonic flutter is weakly dependent upon angle of attack, as opposed to transonic flutter. For truly linear aeroelasticity, there is in fact no dependence between flutter and angle of attack, given the ability to separate static and dynamic aeroelastic physics.[24]

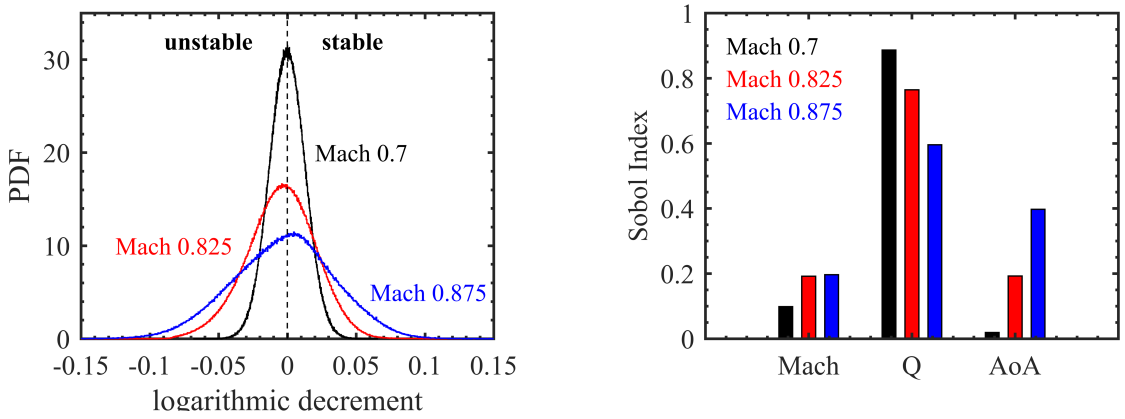

Figure 6. Probability distribution functions (left) and Sobol indices (right) for the three PCEs in Table 1.

An additional technique, which evaluates the ability of the PCEs to emulate the sampled physics, is to compute the flutter boundaries directly from the polynomial surrogate function in Eq. 1. This is shown in Fig. 7, for comparison with the deterministic data repeated from Fig. 4. PCE-derived flutter boundaries are also shown at -2° angle of attack, for which no direct deterministic data exists. These surrogate flutter boundaries match the deterministic data points fairly well, with some exceptions. At Mach number 0.78, the 2° and -2° PCE boundaries are clearly under-fit (bias error), though the 0° model shows a smoother transition from the Mach 0.7 PCE to the Mach 0.825 PCE. Furthermore, all of the models entirely miss the highly nonlinear flutter boundaries at Mach 0.9, which would require a very high order polynomial to fit, particularly at 2° angle of attack.

It is finally noted that, according to the PCE, the response of the -2° surrogate is the most critical in Fig. 7, with a flutter dip below the 15% margin line near Mach 0.88. There is no deterministic data in this area to verify this trend, however, and it is known from the higher angles of attack that the quality of the PCE fit deep in the transonic range is only moderate.

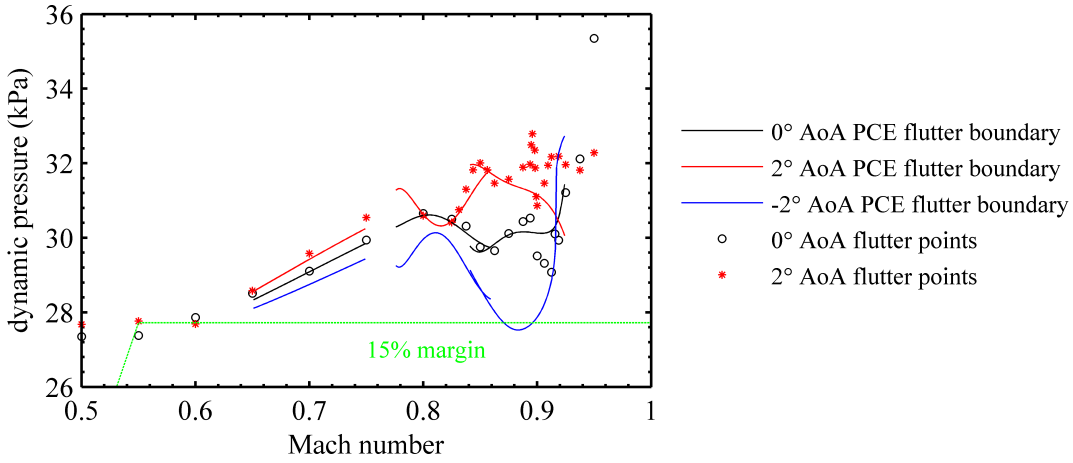

Figure 7. Flutter boundaries predicted with PCE.

V. Atmospheric RVs, Medium CFD Grid

This section repeats the PCE exercise of the previous section, though with the medium CFD grid as opposed to the coarse (13.8 vs. 3.1 million nodes). This is only done for the first subsonic PCE in Table 1, expanded about Mach 0.7. Owing to the weak aeroelastic nonlinearities, the computational burden of this PCE is fairly low; 20 samples for a converged result. Though it would be of great interest to consider a case with mixed flow (i.e., a shock) over the wing, the computational cost for the required high-ordered PCE is too high, at present.

Good agreement in the flutter margin predicted by the two grids can be seen in Fig. 4 at Mach 0.7, with flutter-Q values of 29.10 kPa (coarse) and 29.15 kPa (medium). The logarithmic decrement of the dynamic aeroelastic response is shown in Fig. 8 for all 20 samples, as is the resulting PDF computed from the PCE. As with the deterministic flutter point, the statistical data also matches well between the two grids. It should be noted that the comparison in Fig. 8 is not completely equitable, as the coarse-grid PCE is expanded about a slightly different flutter point than the medium grid (29.10 vs. 29.15 kPa). Differences in resolved flow physics also contribute to the gap in Fig. 8.

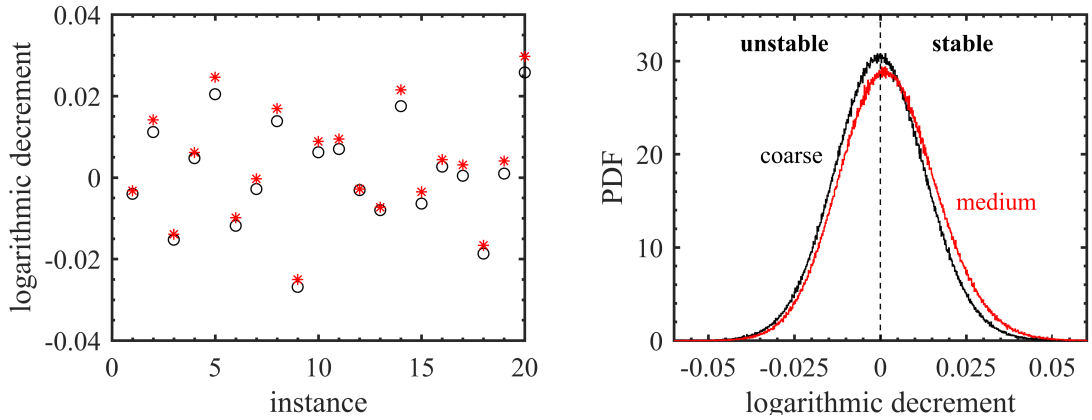

Figure 8. Sampling (left) and PDF computations (right) for the two CFD grids at Mach 0.7.

To this point, only the logarithmic decrement of the dynamic aeroelastic response has been considered

as the response output Y, for PCE generation in Eq. 1. The next result in Fig. 9 considers the pressure coefficient at every point on the CFD surface as an uncertain variable: one second-order PCE per surface grid point (i.e., a multi-output case). This is only done for steady pressures, for both a rigid wing and a flexible wing. The upper contour plots in Fig. 9 show average (μ_Y) pressures, and in the flexible case, these contours are superimposed upon the average wing deformation. Given the near-symmetry of the PDFs in these cases (seen for example in Fig. 8), average pressures will look very similar to deterministic values.

The lower plots in Fig. 9 show slices of pressure data at three span stations, along with 95% confidence intervals (computed from σ_Y). For the rigid wing, the dynamic pressure RV is of minor importance relative to Mach number and angle of attack. Given the matched point atmospheric conditions, Q of a rigid wing will alter the Reynolds number and the flow temperature, but these dependencies upon C_p are minor. For the flexible wing, the Q RV is of course a strong driver due to the aeroelastic re-distribution of loads. Wing twist in Fig. 9 about the elastic axis is small, but bending deformations are larger, and positive bending of a swept wing will decrease the effective angle of attack.[24] This shedding of outboard airloads is clearly seen in Fig. 9.

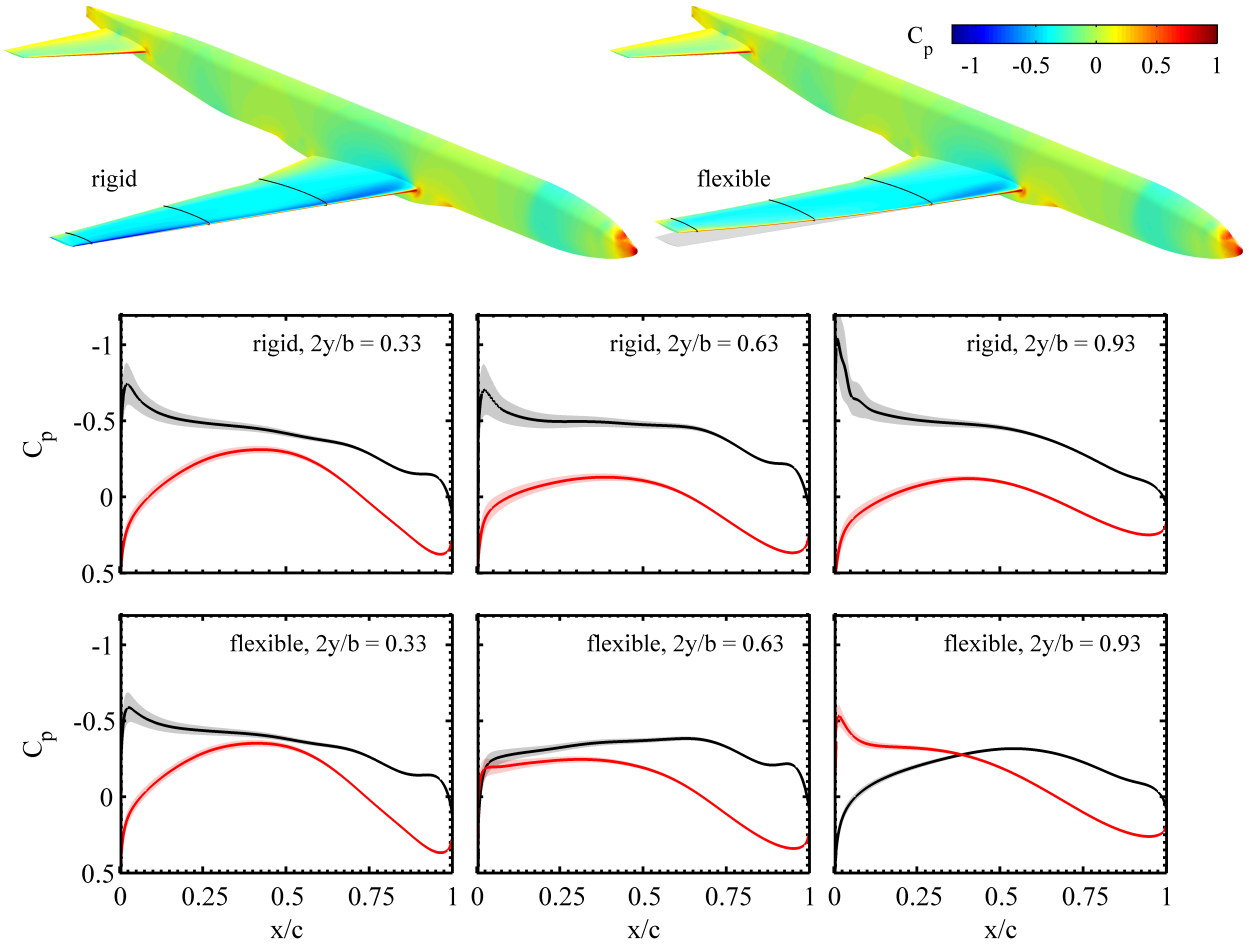

Figure 9. Average rigid and flexible static pressure distributions (top row), and pressure slices with 95% confidence intervals (bottom rows).

As noted, there is no shock in the flow data of Fig. 9, at Mach 0.7. Peak uncertainties, implied by the confidence intervals (computed via μ_Y), therefore occur near the leading edge (as opposed to a transonic condition, where uncertainties would presumably be largest near the shock) of the upper surface. Overall uncertainty levels are higher for the rigid wing than for the flexible wing. This is perhaps surprising given the random fluctuations in wing shape that will be found in the flexible case, and also given that one of the three RVs (Q) has almost no impact on the output uncertainty of the rigid wing. A likely cause for this result is the load-alleviating nature of the swept flexible wing, which can passively adapt to fluctuations in Mach, angle of attack, and Q, whereas the rigid wing cannot. The inclusion of trim loads, which are not

considered here (i.e., C_L is not the same between the rigid and flexible cases), may demonstrate a more even level of uncertainty between the rigid and flexible wings.

VI. Atmospheric, Structural, and Inertial RVs, Coarse CFD Grid

The final section in this paper reverts back to the coarse CFD mesh, but expands the list of random variables. These include: 1) Mach number, 2) angle of attack, 3) dynamic pressure, 4) inboard skin thickness, 5) outboard skin thickness, 6) inboard spar thickness, 7) outboard spar thickness, 8) rib thickness, 9) leading edge mass, 10) trailing edge mass, and 11) engine mass. Each random variable is normally-distributed, and defined as follows:

- Atmospheric RVs (Mach number, angle of attack, dynamic pressure): these are repeated from Table 1, using the expansion about Mach 0.7.
- Structural thickness RVs (inboard and outboard skin thickness, inboard and outboard spar thickness, and rib thickness): the mean values for these variables are the patchwise distributions seen in Fig. 2, with a 0.04 COV. For a given RV (e.g., inboard spar thickness), each of the patchwise values in that set are assumed to randomly scale up or down in tandem, perfectly correlated. In reality, each patch will have its own probability distribution with varying degrees of correlation to adjacent patches, but the current assumption is required to keep the number of RVs low.
- Inertial RVs (leading edge, trailing edge, and engine lumped mass): as above, the mean values (μ) are set to the deterministic values used previously (graphically shown in Fig. 1, with a total engine mass of 5,200 kg, total leading edge mass of 1,200 kg, and trailing edge mass of 2,470 kg), with a 0.04 COV. Each lumped mass attached to a given RV scales up or down in tandem.

The structural sizing RVs can impact both elastic and inertial properties of the wing, with inboard thickness having a greater impact on wing stiffness, and outboard thickness a greater impact on inertial properties. The lumped inertial mass RVs have no stiffness contribution. In order to properly account for the aeroelastic trends due to structural and inertial parameterizations, the NASTRAN model is rerun for each sample (to compute vibration frequencies, mode shapes, and self-weight terms), prior to exercising FUN3D.

These eleven RVs are characterized with a 2^{nd}-order PCE built upon 80 samples. Though not shown here, PCE-based statistical output from a 40-sample model compares well to the 80-sample model, suggesting adequate convergence. Sobol indices for three outputs metrics (computed from three separate PCEs) are shown in Fig. 10: the vibration frequency of the first bending mode (wind-off), the static aeroelastic tip deflection, and the dynamic aeroelastic logarithmic decrement. The bending frequency metric is not an aeroelastic quantity, and so the atmospheric RVs have no contribution. Inboard skin thickness is the main driver here, and the outboard inertial properties (leading/trailing edge lumped mass, outboard skin thickness) have a secondary role. It is important to note that the first bending mode does not typically become the fluttering mode (in wind-on conditions) for these cases. The fluttering mode is usually mode three; a torsional mode with a high degree of engine pitch.

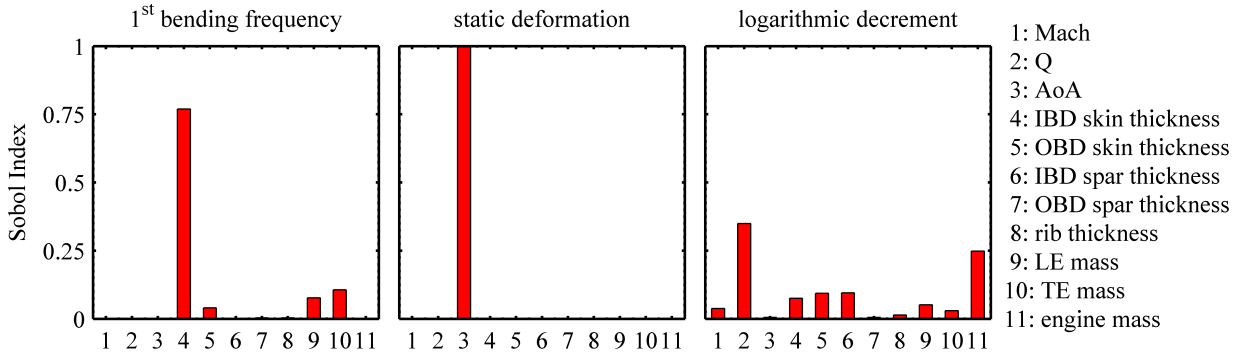

Figure 10. Sobol indices for various response outputs: first bending frequency (wind-off), static aeroelastic tip deformation, and dynamic aeroelastic logarithmic decrement.

The statistical behavior of the second metric in Fig. 10, the static aeroelastic wingtip deflection (cf., seen graphically in Fig. 9), is overwhelmingly driven by the angle of attack RV. In theory, all eleven RVs

will contribute to static aeroelastic deflections through changes in aerodynamic, inertial, or elastic force balancing. The uncertainties in angle of attack, however, are extremely large, with a standard deviation of 1°. For transonic flutter, this range of uncertainty places the angle of attack RV on roughly the same level of importance as the other RVs. For static aeroelastic effects, however, such a distribution monopolizes the probabilistic response, in comparison to a 0.04 COV on skin thickness (for example).

The final metric in Fig. 10, the dynamic aeroelastic logarithmic decrement, is computed as discussed in the previous sections. This metric has a more even spread of Sobol indices, with dynamic pressure and the engine mass constituting the main drivers (as noted, the flutter mode shape is characterized by engine pitch), and structural thicknesses playing a secondary role. Angle of attack in this case has a very small Sobol index owing to the subsonic flow conditions (Mach 0.7), as also seen in Fig. 6.

For this eleven-RV case, a relationship between flutter margin and flutter probability is shown in Fig. 11, in the form of a cumulative distribution function. For the commonly-considered 15% flutter margin (shown in Fig. 4 and Fig. 7), the probability that the wing will flutter within this margin, at Mach 0.7, is 0.202. Referencing back to the Introduction of this paper, the more important question is: what is the probability that the wing will flutter within the flight envelope (i.e., the probability that the flutter margin will be less than zero)? As noted, a long-term goal is to replace the 15% flutter margin with a UQ-driven P_f threshold. As seen on the log-scale plot of Fig. 11, the current PCE does not have enough information within the tail of the failure function to accurately compute this 0%-margin P_f value. A Monte Carlo sampling of the PCE computes P_f as $4 \cdot 10^{-7}$, though a simple moment projection[19] estimates P_f as $2.2 \cdot 10^{-8}$.

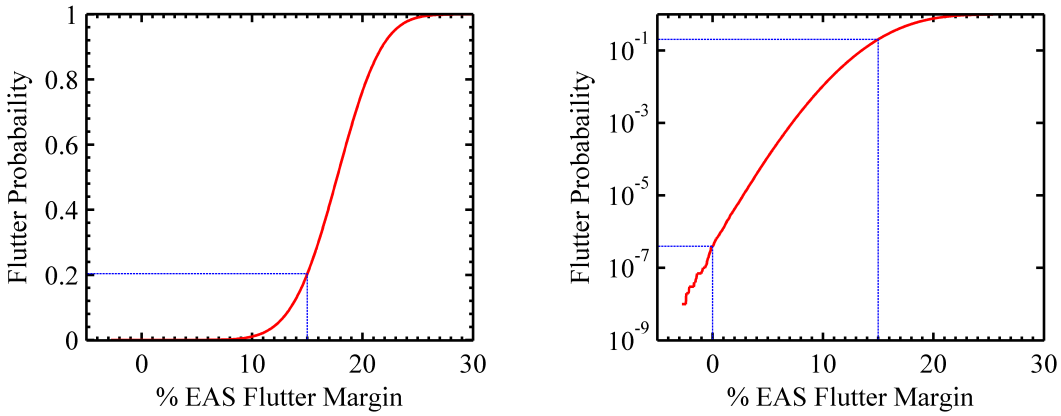

Figure 11. Cumulative distribution function of flutter probability vs. flutter margin (linear scale on left, log scale on right).

VII. Conclusion

This work has conducted an uncertainty quantification analysis of the Common Research Model with a flexible wingbox, using FUN3D and NASTRAN. The main output metric of interest is the damping character of the dynamic aeroelastic wing response (logarithmic decrement), due to some perturbation: this metric will be exactly zero at the flutter point. Secondary metrics include steady pressures, structural displacements, and structural vibration frequencies. A nonintrusive sparse PCE is used to propagate uncertainties through the aeroelastic model, with atmospheric, structural, and inertial RVs all considered. Finally, two CFD meshes are included in this work: a coarse grid (3.1 million nodes) and a medium grid (13.8 million nodes).

For fully subsonic flow conditions, the flutter mechanism is essentially linear. Computationally inexpensive low-ordered PCEs provide accurate representations of the statistical aeroelastic output. Relatively large numbers of random variables can be included in these models, and it is expected that the eventual inclusion of aeroelastic adjoint-based sensitivities in FUN3D can be used to drive the sampling cost down even further.[22] For transonic flows, on the other hand, the CRM exhibits strong nonlinearities, with rapid undulations in the flutter margin across dynamic pressures. The polynomial-based surrogate PCE does not perform as well here, with larger sampling costs needed to approximate the aggressive curvature in the random parameter space. Sparse approximations[12] can be used to temper costs, but plotting the deterministic transonic flutter margins alongside the PCE-derived margins still reveals gaps between the two.

The ultimate goal of this work is to replace the typical 15% flutter margin, frequently used in design work, with a rigorous failure probability threshold.[3] Beyond the typical challenges associated with reliability-based UQ (i.e., how to quantify input uncertainties, how to ascertain an appropriate P_f constraint boundary, how to propagate uncertainties through the physical model, how to compute adjoint sensitivities of P_f for design work, etc.), a transonic flutter constraint is particularly problematic, given the strong nonlinearities at the critical point in the random variable space: the transonic flutter dip. UQ tools with more localized support throughout the random variable space (such as stochastic collocation[3,19]), as opposed to the global basis functions used here, may provide greater accuracy for strongly nonlinear aeroelastic systems.

Acknowledgments

This work is funded by the NASA Advanced Air Transport Technologies project.

References

[1]Pettit, C., "Uncertainty Quantification in Aeroelasticity: Recent Results and Research Challenges," *Journal of Aircraft*, Vol. 41, pp. 1217-1229, 2004.

[2]Timme, S., Badcock, K., "Transonic Aeroelastic Instability Searches using Sampling and Aerodynamic Model Hierarchy," *AIAA Journal*, Vol. 49, No. 6, pp. 1191-1201, 2012.

[3]Beran, P., Stanford, B., Schrock, C., "Uncertainty Quantification in Aeroelasticity," *Annual Review of Fluid Mechanics*, to appear.

[4]Allen, M., Maute, K., "Reliability Based Shape Optimization of Structures Undergoing Fluid-Structure Interaction Phenomena," *Computer Methods in Applied Mechanics and Engineering*, Vol. 194, No. 30, pp. 3472-3495, 2005.

[5]Beran, P., Pettit, C., Millman, D., "Uncertainty Quantification of Limit-Cycle Oscillations," *Journal of Computational Physics*, Vol. 217, No. 1, pp. 217-247, 2006.

[6]Hosder, S., Walters, R., Balch, M., "Efficient Uncertainty Quantification Applied to the Aeroelastic Analysis of a Transonic Wing," *AIAA Aerospace Sciences Meetings and Exhibit*, Reno, NV, January 7-10, 2008.

[7]Witteveen, J., Bijl, H., "Effect of Randomness on Multi-Frequency Aeroelastic Responses Resolved by Unsteady Adaptive Stochastic Finite Elements," *Journal of Computational Physics*, Vol. 228, No. 18, pp. 7025-2045, 2009.

[8]Danowsky, B., Chrstos, J., Klyde, D., Farhat, C., Brenner, M., "Evaluation of Aeroelastic Uncertainty Analysis Methods," *Journal of Aircraft*, Vol. 47, No. 4, pp. 1266-1273, 2010.

[9]Marques, S., Badcock, K., Khodaparast, H., Mottershead, J., "Transonic Aeroelastic Stability Predictions under the Influence of Structural Variability," *Journal of Aircraft*, Vol. 47, No. 4, pp. 1229-1239, 2010.

[10]Nikbay, M., Kuru, M., "Reliability Based Multidisciplinary Optimization of Aeroelastic Systems with Structural and Aerodynamic Uncertainties," *Journal of Aircraft*, Vol. 50, No. 3, pp. 708-715, 2013.

[11]Biedron, R., Carlson, J., Derlaga, J., Gnoffo, P., Hammond, D., Jones, W., Kleb, B., Lee-Rausch, E., Nielsen, E., Park, M., Rumsey, C., Thomas, J., Wood, W., "FUN3D Manual: 13.0," NASA TM-2016-219330.

[12]Blatman, G., Sudret, B., "An Adaptive Algorithm to Build Up Sparse Polynomial Chaos Expansions for Stochastic Finite Element Analysis," *Probabilistic Engineering Mechanics*, Vol. 25, pp. 1831-1897, 2010.

[13]Vassberg, J., DeHaan, M., Rivers, S., Wahls, R., "Development of a Common Research Model for Applied CFD Validation Studies," *AIAA Applied Aerodynamics Conference*, Honolulu, Hawaii, August 10-13, 2008.

[14]Kenway, G., Martins, J., Kennedy, G., "Aerostructural Optimization of the Common Research Model Configuration," *AIAA Aviation Conference*, Atlanta, GA, June 16-20, 2014.

[15]Bartels, R., Rumsey, C., Biedron, R., "CFL3D Version 6.4 - General Usage and Aeroelastic Analysis," NASA TM 2006-214301.

[16]Rendall, T., Allen, C., "Efficient Mesh Motion Using Radial Basis Functions with Data Reduction Algorithms," *Journal of Computational Physics*, Vol. 228, pp. 6231-6249, 2009.

[17]Biedron, R., Thomas, J., "Recent Enhancements To The FUN3D Flow Solver For Moving-Mesh Applications," AIAA Paper 2009-1360.

[18]Hosder, S., Walters, R., Balch, M., "Point-Collocation Nonintrusive Polynomial Chaos Method for Stochastic Computational Fluid Dynamics," *AIAA Journal*, Vol. 48, No. 12, pp. 2721-2730, 2010.

[19]Eldred, M., "Recent Advances in Non-Intrusive Polynomial Chaos and Stochastic Collocation Methods for Uncertainty Analysis and Design," AIAA Paper 2009-2274.

[20]Tibshirani, R., "Regression Shrinkage and Selection via the Lasso," *Journal of the Royal Statistical Society, Series B*, Vol. 58, No. 1, pp. 267-288, 1996.

[21]MathWorks, "Statistics Toolbox: User's Guide (R2016b)", retrieved October 2016 from "http://www.mathworks.com/help/pdf_doc/stats/stats.pdf"

[22]Roderick, O., Anitescu, M., Fischer, P., "Polynomial Regression Approaches Using Derivative Information for Uncertainty Quantification," *Nuclear Science and Engineering*, Vol. 164, pp. 122-139, 2010.

[23]Sudret, B., "Global sensitivity analysis using polynomial chaos expansion," *Reliability Engineering and System Safety*, Vol. 93, No. 7, 2008, pp. 964-979.

[24]Bisplinghoff, R., Ashley H., Halfman, R., *Aeroelasticity*, Addison-Wesley Publishing Co., Reading, MA, 1955.